Estimating and Mapping Mangrove Biomass Dynamic Change Using WorldView-2 Images and Digital Surface Models

Yuanhui Zhu [ID], Kai Liu [ID], Lin Liu, Soe W. Myint, Shugong Wang, Jingjing Cao, and Zhifeng Wu

Abstract—Mapping and quantification of biomass changes is critical to understanding mangrove carbon sequestration, conservation, and restoration. Few previous studies have focused on mangrove biomass changes based on high spatial resolution images, particularly for disturbed and recovering areas. This study developed an effective model to estimate and map mangrove aboveground biomass dynamic change between 2010 and 2016 on Qi'ao Island in South China. The study area includes native *Kandelia candel* (*K. candel*) and planted *Sonneratia apetala* (*S. apetala*) mangrove species within the largest planted area in China. Models were developed using WorldView-2 images, digital surface models (DSMs), and the random forest algorithm. Accuracies of the model were assessed using multiyear field samples. DSMs were identified as the most important variable for model accuracy, reducing relative error by up to 3.14%. Three models were developed: a model for 2010, another model for 2016, and a combined model for 2010 and 2016. Compared with the 2010 (RMSE = 41.03 t/ha, RMSEr = 24.31%) and 2016 (RMSE = 39.92 t/ha, RMSEr = 23.40%) models, the combined model (RMSE = 50.99 t/ha, RMSEr = 30.48%) only increased the relative error by 6.17% and 7.08%, respectively. Mangrove biomass maps generated from the most accurate models showed total biomass increased from 23270.43 to 39819.03 tons by up to 71.11% over the study period. *K. candel* total biomass decreased by 36.5% due to Derris trifoliata challenge. *S. apetala* total biomass increased by 74.79% due to reforestation programs, achieving aboveground biomass accumulation of 4.17 t/ha for stands that existed in 2010. This study provides insights into biomass dynamic change in disturbed and recovering mangrove areas. Future studies should consider using LiDAR techniques to obtain actual tree height applied for biomass estimation instead of DSM.

Index Terms—Biomass change, digital surface models (DSMs), mangrove species, WorldView-2 images.

Yuanhui Zhu is with the Center of GeoInformatics for Public Security, School of Geographical Sciences, Guangzhou University, Guangzhou 510006, China (e-mail: zhuyhui2@gzhu.edu.cn).

Lin Liu is with the Center of GeoInformatics for Public Security, School of Geographical Sciences, Guangzhou University, Guangzhou 510006, China, and also with the Department of Geography, University of Cincinnati, Cincinnati, OH 45221-0131 USA (e-mail: liulin1@gzhu.edu.cn).

Kai Liu and Jingjing Cao are with the Guangdong Provincial Engineering Research Center for Public Security and Disaster, Guangdong Key Laboratory for Urbanization and Geo-simulation, School of Geography and Planning, Sun Yat-sen University, Guangzhou 510275, China (e-mail: liuk6@mail.sysu.edu.cn; caojj5@mail.sysu.edu.cn).

Soe W. Myint is with the School of Geographical Sciences and Urban Planning, Arizona State University, Tempe, AZ 85287 USA (e-mail: Soe.Myint@asu.edu).

Shugong Wang is with the Guangdong Key Laboratory of Geological Processes and Mineral Resources Survey, School of Earth Science and Geological Engineering, Sun Yat-sen University, Guangzhou 510275, China (e-mail: esswsg@mail.sysu.edu.cn).

Zhifeng Wu is with the Guangdong Province Engineering Technology Research for Geographical Conditions Monitoring and Comprehensive Analysis, School of Geographical Sciences, Guangzhou University, Guangzhou 510006, China (e-mail: gzuwzf@163.com).

Digital Object Identifier 10.1109/JSTARS.2020.2989500

I. INTRODUCTION

MANGROVE forests grow in coastal, estuary, and river intertidal zones in tropical and subtropical regions [1], [2]. As continental marine transitional ecosystems, they provide essential ecosystem goods and services. One important function is global warming mitigation due to highly effective carbon sequestration compared with other terrestrial ecosystems [3]. Consequently, climate warming mitigation programs often include mangrove forest programs, such as Reducing Emissions from Deforestation and Forest Degradation (REDD+) [4], [5], Payments for Ecosystem Services (PES), and Blue Carbon [6]. Those require accurate monitoring and mapping for baseline carbon stock and to validate conservation efforts. Aboveground biomass (AGB) is a critical carbon metric for mangrove ecosystems [7].

Previous studies have shown large mangrove ecosystem reductions and conversions into aquaculture, rice cultivation, and human settlement over the past few decades due to population pressure and rapid urban growth [8]. This is particularly true for China, where more than 68.7% of mangrove forests were depleted before the late 1990s [9]. Since then, many restored planting schemes have been implemented. Therefore, it is crucial to map spatio-temporal dynamic changes in mangrove biomass to assess and understand regional carbon cycles and planting effects. Moreover, mapping mangroves are essential for coastal management, spatial planning, and decision making [10].

Few studies have focused on monitoring mangrove forest AGB changes using high-resolution images due to limitations in obtaining sample information, mangrove's tardy growth rate, and maintaining AGB stability over time [11]–[13]. However, artificially restored areas (i.e., from planting fast-growing species)

promoted their rapid changes in AGB distribution spatially and temporally [14]. Studies that focus on AGB changes in these areas are required to quantify biomass carbon accumulation and provide insights into artificial restoration effects. However, previous studies usually concentrated on field measurements [14], [15] since remote sensing-based models to assess and monitor mangrove biomass are significantly constrained by the number of samples that are usually limited [13]. Therefore, combining all samples over different years to produce a larger dataset is critical in building operational and effective AGB models.

Vegetation biomass represents all organic matter produced from living plants [16] and can often be effectively estimated by allometric models used to measure tree height, diameter at breast height (DBH), species type, and growth density in a quadrat [9], [17]. Optical images can be used to estimate forest biomass because they quantify vegetation response to electromagnetic waves, reflecting growth density and vegetation status [17]–[19]. SAR images are more effective in estimating forest biomass due to their independence of clouds and deriving canopy structure by actively emitting radiation to detect and measure branches and trunks [20]. Producing accurate biomass models requires further key input parameters that can be obtained from images, such as species type and tree height, to identify variations of a mangrove forest structure [21]. Species type can be mapped by supervised classification [22], [23], and tree height can be obtained by canopy height models (CHM) using LiDAR (e.g., satellite LiDAR [24], terrestrial LiDAR [25], airborne LiDAR [26]), InSAR [26]–[29], or aerial photographs [30]–[33], which can be successfully applied to estimate forest biomass.

Recent progress enables effective CHMs from 3-D point clouds using the Structure from Motion (SfM) photogrammetry algorithm from aerial photographs [34], [35]. SfM is a photogrammetric technique to rebuild 3-D structures from overlapping images that is most suited to unmanned aerial vehicle (UAV) images with their high degree of overlap to capture DSM of the scene [36]. It is also an adequate low-cost alternative to obtain tree height compared with LiDAR or InSAR methods [37]. Previous studies demonstrated the utility of CHM derived from SfM [25], [38], [39], which has also been applied to estimate AGB [30]–[33].

CHM is usually calculated from the corresponding digital surface model (DSM) by subtracting the digital terrain model (DTM) based on point cloud data. However, CHM for dense mangrove forests is not yet fully functional since point clouds from SfM photogrammetry and aerial photographs are incapable of penetrating dense forest canopies to obtain DTMs [40]. Therefore, few studies have considered mangrove AGB estimation using SfM and aerial photographs [40]–[42]. Since mangrove forests mainly grow over even terrain [40], it can be anticipated that DSM can effectively estimate mangrove AGB by using relative mangrove tree heights instead of CHM. However, the utility of such a method for mangrove AGB remains uncertain.

Mangrove species types should be emphasized to improve biomass estimation accuracy due to their significant spectral signature differences [9], [43]. They can be obtained by object-based or pixel-based classification approaches [44]. Object-based classification is the process of dividing images into groups of pixels (objects) with homogeneous and spatially contiguous regions [45], [46], rather than the pixel-based classification. Each object is produced by aggregating pixels with a spatial neighborhood and similar features, thereby reducing the variability. Previous studies have demonstrated that object-based classification is better suited to identifying mangrove forests as they have relative homogeneous canopy for specific species and usually form discrete units [44], [47], [48]. Different data sources (e.g., optical or SAR) have used the object-based method to map mangrove species classification and improved accuracies compared to the pixel-based method [44], [49].

Statistical models are used in building remote sensing-based models to retrieve forest biomass, which include multiple linear regression and machine learning [19]. Machine learning algorithms as a statistical model were commonly used to estimate biomass due to their fewer assumptions for the data and processes and higher estimation accuracies than linear regression in most cases [50]. The random forest (RF) regression algorithm as an ensemble learning technique is one of the popular machine learning algorithms [50]. A major advantage of the RF model is that it reduces the algorithm's risk for overfitting due to relative insensitivity to variations in parameter values. Some studies have demonstrated that it performs good predictive capabilities for biomass estimation [13], [51].

Further study is required to estimate and map spatio-temporal dynamics of mangrove biomass at the species level for mainly reforested areas. Uncertainty remains regarding the effects of DSM variables from the SfM algorithm, and combing samples from different years on the accuracy of biomass estimation. Therefore, the current study developed an effective model to estimate biomass and map mangrove biomass dynamic change from WorldView-2 images and aerial photographs. The specific objectives are threefold:

1) evaluation of the effectiveness of DSM data from aerial photographs for mangrove AGB retrieval and mapping;
2) exploration of the effects of combining samples from different years on AGB estimation;
3) analysis of spatio-temporal mangrove biomass dynamic change at the species level in an intensively restored area.

II. Study Area and Materials

A. Study Area

Qi'ao Island (22°23′N–22°27′N, 113°36′E–113°39′E), located in the eastern Zhuhai city, Guangdong Province (see Fig. 1) [44], is a rare mangrove area close to a large city in China that provides a cross-border channel for migratory birds. The study area has a subtropical monsoon climate with a mean annual temperature of 22.4 °C, sunshine hours of 1907.4 h, and rainfall totaling 1700–2200 mm [52]. Surface seawater salinity ranges from 0.22% to 32.32% with an annual average of 18.22% [52], with irregular semidiurnal tidal pattern. The soil is mostly argillaceous sediment. Hence, the island environment is very suitable for mangrove growth. Mangrove forests mainly grow in Dawei Bay of northwest Qi'ao Island. This area is the largest restored conservation area for mangrove forests in
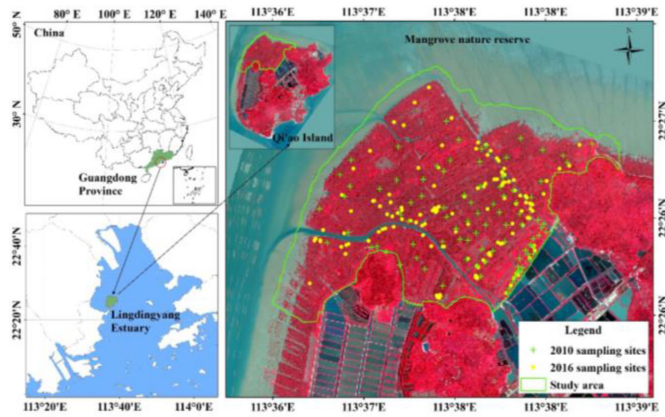
Fig. 1. Study area and field measurement sites overlaid on a Worldview-2 images (bands 7, 5, and 3 false color combination) in 2016 on Qi'ao Island.

China, covering approximately 700 ha, and was recognized as a provincial level nature reserve in 2004 [53], [54].

Qi'ao Island previously had large mangrove forest areas due to its ideal setting and extensive mudflats [43]. However, they were reduced to only 0.32 km² by 1998 due to intertidal zone reclamation, and hence, artificial planting was implemented to restore mangrove forests [43]. Thus, the study area can be characterized by external disturbances and recovery [55].

The primary mangrove species consisted of *Kandelia candel* (*K. candel*), *Sonneratia apetala* (*S. apetala*), *Aegiceras corniculatum* (*A. corniculatum*), *Acanthus ilicifolius* (*A. ilicifolius*), and *Acrostichum aureum* (*A. aureum*) on Qi'ao Island. We focused on prevalent mature and native *K. candel* and restored *S. apetala* based on uneven aged mangrove forests. *K. candel* and *S. apetala* are the primary mangrove species on Qi'ao Island. *K. candel* is largely concentrated outside the enclosing levee in high tidal zones. The stand had a mean age over 45 years and tree height ranging from 5.5 to 7.5 m. The restored *S. apetala* species originated in Bangladesh and was first planted on Qi'ao Island in 1999. The *S. apetala* species covers almost the entire study area except around the levee. *S. apetala* is fast-growing and has a tree height ranging from 4 to 21 m, with an increasing rate at approximately 1.5 m each year in early growing stages. The afforestation sequence was executed from the shore seaward over time.

B. Field Investigation

Mangrove species types and biomass were gathered by field investigations in 2010 and 2016. A total of 683 and 722 samples of mangrove species were collected over the study area by field investigation and UAV images with 0.12 m resolution. Half of the samples were used for model training and the remaining for validation. A total of 91 biomass samples were obtained in 2010, including 68 restored *S. apetala* plots and 23 native mature *K. candel* plots, whereas 144 samples were collected in 2016, including 133 *S. apetala* plots and 11 *K. candel* plots, respectively. Sampling locations covered most of the study area, ensuring all biomass variations due to the tree age and crown cover were evenly represented. Each sample plot was a 10

TABLE I
ALLOMETRIC EQUATIONS OF MANGROVE SPECIES BASED ON DBH AND HEIGHT

Species	Tissues	Allometric Equations	Correlation
S. apetala	Foliage	$\lg W_{lf} = -0.756 + 0.4355$ $\lg(DBH^2 \times Height)$	0.94
	Branch	$\lg W_{br} = 0.1590 + 0.3879$ $\lg(DBH^2 \times Height)$	0.95
	Trunk	$\lg W_{st} = 0.3067 + 0.3302$ $\lg(DBH^2 \times Height)$	0.95
	Bark	$\lg W_{ba} = -0.3790 + 0.3559$ $\lg(DBH^2 \times Height)$	0.91
	Flowers and fruit	$\lg W_{fr} = -2.3456 + 0.3791$ $\lg(DBH^2 \times Height)$	0.97
K. candel	Foliage	$\lg W_{lf} = -1.1704 + 0.4855$ $\lg(DBH^2 \times Height)$	0.87
	Branch	$\lg W_{br} = -0.9067 + 0.5762$ $\lg(DBH^2 \times Height)$	0.95
	Trunk and bark	$\lg W_{st+ba} = -0.3112 + 0.2542$ $\lg(DBH^2 \times Height)$	0.88
	Flowers and fruit	$\lg W_{fr} = -3.1582 + 1.061$ $\lg(DBH^2 \times Height)$	0.85

TABLE II
CHARACTERISTICS OF WORLDVIEW-2 IMAGES

Sensors	Resolution	Bands	Wavelength range(nm)
WorldView-2	2m of the multispectral bands	Coastal band	450 − 510
		Blue band	510 − 580
		Green band	630 − 690
		Yellow band	770 − 895
		Red band	400 − 450
		Red-edge band	585 − 625
		Near-infrared 1 band	705 − 745
		Near-infrared 2 band	860 − 1040
	0.5m of the panchromatic band		450 − 800

× 10 m quadrat. Tree height was measured using a handheld laser range finder (Trueyard SP-1500H, Trueyard Optical Instruments Company), and DBH was recorded for each living tree along with the number of living trees for each plot. Only trees with DBH above 5 cm were recorded. Submeter accurate GPS was used to record the quadrat center and vertices of each sample. We also recorded auxiliary details including distances to shore and other recognizable features using WorldView-2 images and aerial photographs to locate sites on the images. The above-ground biomass for each plot was calculated from species-specific allometric equations for the study area, as listed in Table I [56].

C. Data Collection and Processing

1) WorldView-2 Images: Two WorldView-2 images were obtained with 2-m spatial resolution for biomass estimation from 11 November 2010 and 29 July 2016, as detailed in Table II. Both images included eight multispectral bands: four traditional bands (blue, green, red, and near infrared 1) and four new bands (coastal, yellow, red-edge, and near-infrared 2).

Preprocessing including geometric correction was performed using 15 ground control points conformed to a UTM Zone
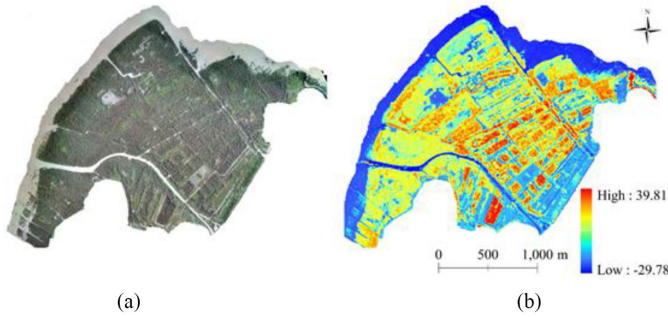
Fig. 2.   (a) DOM and (b) DSM maps derived from aerial photographs in 2016.

Fig. 3.   Workflow diagram to estimate mangrove AGB based on WorldView-2 images and DSMs.

49 map projection followed by a resampling procedure using the nearest neighbor approach. The root-mean-square error (RMSE) of geometric correction was less than 0.5 pixel (1 m) for both images. Radiometric calibration was achieved through calibration utilities to convert digital numbers into radiance values, and then surface reflectance was obtained by atmospheric correction using fast line-of-sight atmospheric analysis of the spectral hypercubes (FLAASH) model with the ENVI module.

2) UAV Images: We only collected UAV images in 2016 from a fixed wing UAV with onboard GPS/inertial measurement unit, 80% frontal overlap, and 60% side overlap at 400 m altitude. The images (RGB, 4912 × 3264 pixel) were captured with a SONY NEX-5T camera with geolocation (latitude/longitude with WGS84 horizontal) and altitude (EGM96 vertical datum for the frame center) embedded in the EXIF data.

The original images were processed to generate DSMs and digital orthophoto maps (DOMs) using Agisoft PhotoScan Professional (64 bit) software (AgiSoft LLC) [57]. Overlapping photographs were used to generate DSM and DOM maps of the study area based on the SfM algorithm [39], [58]. The SfM algorithm acquires a 3-D point cloud similar to those from LiDAR data by standard automated techniques using computer vision and traditional stereoscopic photogrammetry [59]. It has a high level of automation and great ease of use. It has been reported that the accuracy of photogrammetrically generated DSMs depends on geometric and physical parameters, such as the image scale, ground sampling density, and so on [60]. Usually, high-resolution DSMs from UAVs imagery and SfM algorithm with accuracy better than 10 cm can meet our research requirement [60].

Agisoft PhotoScan software was used to reconstruct the ground surface to get the DSMs, including the following steps [61]. Images were first aligned using a scale-invariant feature transform algorithm to detect image features, such as edges or other geometrical features, and reconstruct their movement through the image sequence [62]. Pixel-based stereo reconstruction was then executed on the aligned images, and then fine topographic products were meshed using a texture method. The resultant DSM and DOM maps were exported at 0.12 m resolution (see Fig. 2), and geometric correction applied from ground control points and the nearest neighbor approach. DSMs were resampled at 2-m resolution to correspond to WorldView-2 images.
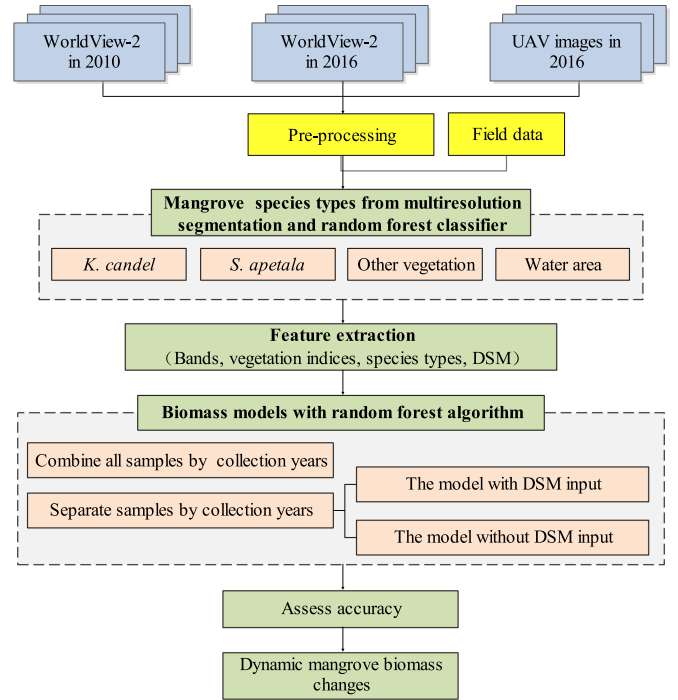
III. METHODOLOGY

The RF algorithm was applied to WorldView-2 images to obtain mangrove forest AGB for 2010 and 2016. An accurate estimation of AGB requires a range of inputs, including spectral features, species types, and tree height. Spectral features and species types were obtained from the WorldView-2 images, and tree heights from DSMs based on the UAV-SfM algorithm. Fig. 3 shows the workflow overview, and details are discussed in subsequent sections.

A. Species Classification and AGB Estimation Algorithm

We used the RF algorithm, an ensemble learning method that works by constructing multiple decision trees, for species classification and biomass estimation [50]. The RF algorithm combines bootstrap aggregating and random feature selection to construct decision trees (n_{tree}) with controlled variance [50]. Each node of the trees splits using a random subset of input variables (m_{try}). RF also corrects for a decision tree overfitting the training set and has high robustness to outliers and noise. Out-of-bag (OOB) is used to estimate the generalization error for the RF model utilizing bootstrap aggregating to subsample data samples used for training. Usually, the RF algorithm uses 2/3 of the samples as "in-bag data" by random selection to grow up each tree and build the model, and the remaining samples (1/3 of the samples) as "out-of-bag data" to measure the model's error [63], [64]. The RF process involved the following steps.

1) Bootstrap samples from the training datasets were used to generate *n* new training datasets of equal size to the observed datasets by random sampling with replacement from the original training datasets.

2) Multiple decision trees (n_{tree}) were constructed based on the bootstrap samples. Each tree node was split using a random subset of input variables (m_{try}). Random predictive variable selection reduces correlation among decision trees and generalization error [63].

3) The final prediction was determined by averaging the decision trees. Tuning parameters (n_{tree} and m_{try}) were searched using grid search to obtain optimized model parameters providing the highest accuracy.

Model building, tuning, and accuracy evaluations were performed using the R statistical environment and "randomForest" package [65]. The importance of each variable was calculated using the mean decrease in accuracy (MDA), i.e., the OOB error difference between the original data set and a dataset with randomly permuted variables.

B. Calculation of Vegetation Indices

Vegetation indices (VIs) and the eight WorldView-2 image bands were input to the biomass estimation models. In this study, ρ_{B1} (coastal band), ρ_{B5} (red band), ρ_{B6} (red-edge band), ρ_{B7} (near-infrared-1 band), and ρ_{B8} (near-infrared-2 band) of the WorldView-2 images were used to calculate nine VIs, including the normalized difference vegetation index (NDVI), the simple ratio index (SRI), the difference vegetation index (DVI), red-edge NDVI (RE-NDVI), red-edge SRI (RE-SRI), and modified red-edge SRI (mRE-SRI) [9], 66]. These VIs have been proven to successfully estimate vegetation parameters that could be crucial for AGB estimation [66]. They are commonly related to canopy foliage content, vegetation status, and canopy structure [67]. The indices are computed as follows:

$$\text{NDVI}_{75} = \frac{\rho_{B7} - \rho_{B5}}{\rho_{B7} + \rho_{B5}} \tag{1}$$

$$\text{NDVI}_{85} = \frac{\rho_{B8} - \rho_{B5}}{\rho_{B8} + \rho_{B5}} \tag{2}$$

$$\text{SRI}_{75} = \frac{\rho_{B7}}{\rho_{B5}} \tag{3}$$

$$\text{SRI}_{85} = \frac{\rho_{B8}}{\rho_{B5}} \tag{4}$$

$$\text{DVI}_{75} = \rho_{B7} - \rho_{B5} \tag{5}$$

$$\text{DVI}_{85} = \rho_{B8} - \rho_{B5} \tag{6}$$

$$\text{RE} - \text{NDVI}_{65} = \frac{\rho_{B6} - \rho_{B5}}{\rho_{B6} + \rho_{B5}} \tag{7}$$

$$\text{RE} - \text{SRI}_{65} = \frac{\rho_{B6}}{\rho_{B5}} \tag{8}$$

$$\text{mRE} - \text{SRI}_{651} = \frac{\rho_{B6} - \rho_{B1}}{\rho_{B5} + \rho_{B1}}. \tag{9}$$

C. Mapping Mangrove Species

Species information was treated as a dummy variable to the AGB estimation models. The built regression models are easy to interpret when dummy variables are limited to specific values. Mangrove species classification maps were generated
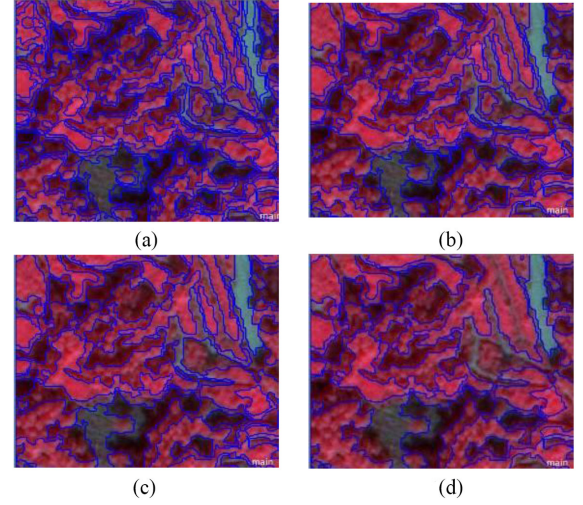

Fig. 4. Segmentation scales (a) 30, (b) 60, (c) 80, and (d) 100 for WorldView-2 images false color combination (bands 7, 5, and 3).

using an object-based classification and RF algorithm. Due to their homogeneous distribution, target objects in the study area, including *S. apetala* and *K. candel*, were hard classified with the RF classifier.

1) Image Segmentation: Image segmentation was required for object-based mangrove species classification [68]. Image objects for each scene were generated using a multi-resolution segmentation algorithm in eCognition Developer 9.0 [69], which is a bottom-up region merging method. The algorithm requires a scale parameter to control heterogeneity growth and influence mean image object size. Other parameters [shape index (0.3), color index (0.7), compactness index (0.4), and smoothness index (0.6)] were set to optimize segmentation results. Ideal image object size should match true surface features without over or under segmentation. Fig. 4 compares segmentation outcomes for different scale parameters (30, 60, 80, and 100). We selected a scale parameter of 80 producing the best visual effect matching true surface features.

2) Mangrove Species Classification: After image segmentation, the features of each object were computed as the input variables to train and build the classifier. The features were shown as follows.

1) Eight multispectral and 1 panchromatic WorldView-2 bands for each image object.
2) Nine VIs: NDVI_{75}, SRI_{75}, DVI_{75}, NDVI_{85}, SRI_{85}, DVI_{85}, RE-NDVI_{65}, RE-SRI_{65}, and mRE-SRI_{651}.
3) Eight texture features of panchromatic band: homogeneity, contrast, dissimilarity, mean, variance, entropy, energy, and correlation.
4) Multispectral band transformations: principal component analysis factors (additive contribution up to 85%) and minimum noise fraction (MNF) components (three highest signal-to-noise ratio components).

Finally, an RF algorithm was applied to classify mangrove species using the abovementioned input features and samples of mangrove species.

D. Biomass Modeling and Accuracy Assessment

The eight bands and nine VIs derived from WorldView-2 images were used as the input variables, and the field mangrove AGB measurements were used as the output variable to build RF models. The built RF models were used to predict and map AGB spatial distribution across the whole image. To analyze the effect of mangrove biomass samples over different years on estimation accuracy, two experiments were conducted to build RF models. One model combined all the samples from the two different years to provide larger training and testing datasets. The other two models were built for each individual year to avoid possible spectral differences between capture years. Furthermore, we also explored DSM effects for mangrove AGB estimation using models based on images and samples from 2016.

Model accuracy was calculated using k-fold cross validation due to the limited number of biomass samples. We employed iterated fivefold cross validation, partitioning the samples into five separate datasets of four training samples and one validation sample rather than the common tenfold cross validation, due to limited samples. Each dataset was generated using a stratified random sampling to ensure they contained the whole range of biomass values. Model results for each fivefold cross validation (e.g., RMSE) were calculated for the average over each iterated accuracy estimation. Estimation accuracies were measured by RMSE and relative RMSE (RMSEr) between the measured and predicted values for the validation datasets. Their formulas are as follows:

$$\text{RMSE} = \sqrt{\frac{\sum (y_i - \hat{y}_i)^2}{n}} \qquad (10)$$

$$\text{RMSE}_r = \frac{\text{RMSE}}{\bar{y}} \qquad (11)$$

where y_i ($i = 1, 2, \ldots, n$) and $\hat{y}_i$ represent the measured and predicted value of AGB at plot i based on fivefold cross validation data, respectively, and $\bar{y}$ represents the measured mean of AGB and n is the number of plots.

IV. RESULTS

A. Mangrove Species Classification

The resulting mangrove species maps for 2010 and 2016 are shown in Fig. 5, and the corresponding classification accuracies are shown in Tables III and IV. The overall accuracies of mangrove species classification were 81.12% and 78.83%, respectively. The accuracy in 2010 is superior due to the more complex nature of species composition and mixture in 2016. Overall, the accuracy of the *S. apetala* plantation is superior to *K. candel* since *S. apetala* was artificially planted and more homogeneous. Some native *K. candel* plantations were also covered by *Derris trifoliata* (*D. trifoliata*), leading to more heterogeneity. To meet requirements for follow-up biomass estimation and prediction, the classified maps were manually edited by researchers familiar with the study area based on field investigation, prior knowledge, and higher resolution data (such as UAV 0.12 m resolution). As shown in Fig. 5, *K. candel* plantations were mainly distributed outside the enclosing levee in high tidal zones with specific strips
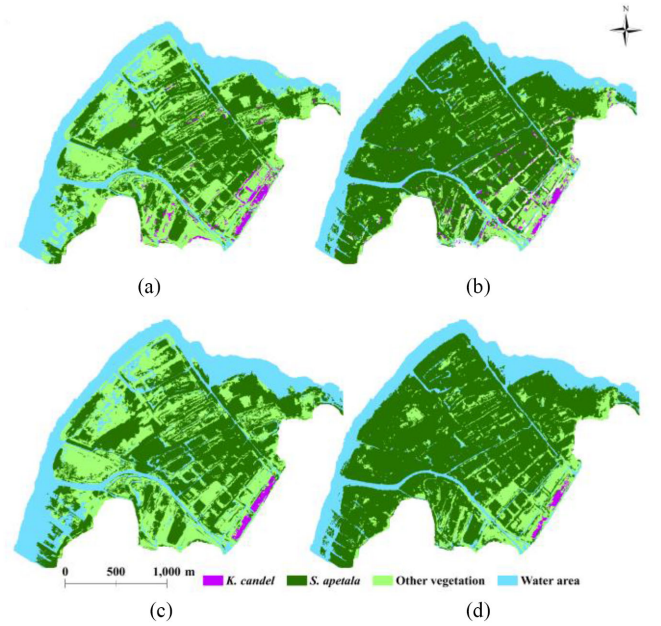

Fig. 5.   Classified mangrove maps for Qi'ao Island originally obtained maps in (a) 2010 and (b) 2016, and the edited maps in (c) 2010 and (d) 2016.

TABLE III
CONFUSION MATRIX OF OBJECT-ORIENTED CLASSIFICATION FOR MANGROVE SPECIES IN 2010

Classified Data	Reference Data				Total	User's Accuracy
	K. candel	*S. apetala*	Other vegetation	Water area		
K. candel	30	4	7	0	41	73.17%
S. apetala	3	115	25	0	143	80.42%
Other vegetation	5	10	93	7	115	80.87%
Water area	0	0	3	37	40	92.50%
Total	38	129	128	44	339	—
Producer's accuracy	78.95%	89.15%	72.66%	84.09%	—	—
Overall accuracy: 81.12; Kappa: 0.723						

in the study area, whereas *S. apetala* plantations were located all over the study area and had the largest area. *S. apetala* plantations showed a sharply increased area (increased by 60.91%) between 2010 and 2016 due to restoration planting.

B. Biomass From Field Sampling

Both mangrove species, *K. candel* and *S. apetala*, were investigated by field survey, as listed in Table V. *K. candel* exhibited higher density with luxuriant foliage and high canopy closures. However, more than 90% of the top canopy was covered by *D. trifoliata*, with understory plants (e.g., *A. ilicifolius*), which are approximately 1 m high. Since the top community was in late ecological succession, the density of *K. candel* gradually reduced by 14.57% between 2010 and 2016. However, average tree height and DBH were similar during this period. Mean AGB decreased from 272.97 t/ha in 2010 to 246.46 t/ha in 2016.

The artificially planting mangrove species, *S. apetala*, grows quickly and was used to inhibit *S. alterniflora*, an invasive alien

TABLE IV
CONFUSION MATRIX OF OBJECT-ORIENTED CLASSIFICATION FOR MANGROVE SPECIES IN 2016

Classified Data	Reference Data					
	K. candel	*S. apetala*	Other vegetation	Water area	Total	User's Accuracy
K. candel	27	6	3	0	36	75.00%
S. apetala	4	125	15	0	144	86.81%
Other vegetation	5	32	90	7	134	67.16%
Water area	0	0	4	41	45	91.11%
Total	36	163	112	48	359	—
Producer's accuracy	75.00%	76.69%	80.36%	85.42%	—	—
Overall accuracy: 78.83; Kappa: 0.686						

TABLE V
BIOMASS OF *K. CANDEL* AND *S. APETALA* OBTAINED FROM THE FIELD SAMPLES ON QI'AO ISLAND

	Year			
	2010		2016	
Species	K. candel	S. apetala	K. candel	S. apetala
Average height(m)	6.62	11.41	6.81	13.64
Average DBH (cm)	8.32	13.23	8.57	14.42
Number of trees per ha	5257	1860	4491	1623
Range of biomass(t/ha)	170.96~448.19	37.44~258.17	169.18~319.69	90.65~301.92
Average AGB(t/ha)	272.97	125.49	246.46	159.7
Standard deviations (t/ha)	67.27	55.23	50.03	43.88

species, since 2000. Understory plants included small tree and shrub species, such as *A. ilicifolius*, *A. aureum*, and *Pluchea indica*. Tree height and DBH increased by 19.54% and 8.99% from 2010 to 2016, respectively, but growing density decreased slightly by 12.74%. Mean AGB increased from 125.49 to 159.70 t/ha between 2010 and 2016.

C. Biomass Estimation Model Accuracies

Biomass estimation models were developed using the RF algorithm, providing sample biomass output from the various inputs (bands and VIs of WorldView-2 images, species types, and DSM). The scatterplots of the predicted versus measured AGB were presented to show the accuracy of the models by the RF algorithm and fivefold cross validation (see Fig. 6). The predicted AGB values of all models were above the 1:1 line in lower measured values, indicating that AGB values of the mangrove plantation were overestimated, but they were the opposite in the higher measured values. Table VI compares biomass estimates for different input variables and sample combinations using mean cross validation RMSE (see Section III-D).

The individual models using separate samples from their respective years exhibited up to 6.17% and 7.08% (RMSEr) improved estimation accuracy for 2010 and 2016 compared to the model using all samples collected in both years (RMSE = 50.99 t/ha, RMSEr = 30.48%). Including the DSM input produced superior accuracy (RMSE = 34.16 t/ha, RMSEr = 20.54%) compared with the other models.

Fig. 7 shows the level of importance of the select variables for AGB estimation in 2010 and 2016 based on 100 replicate RF
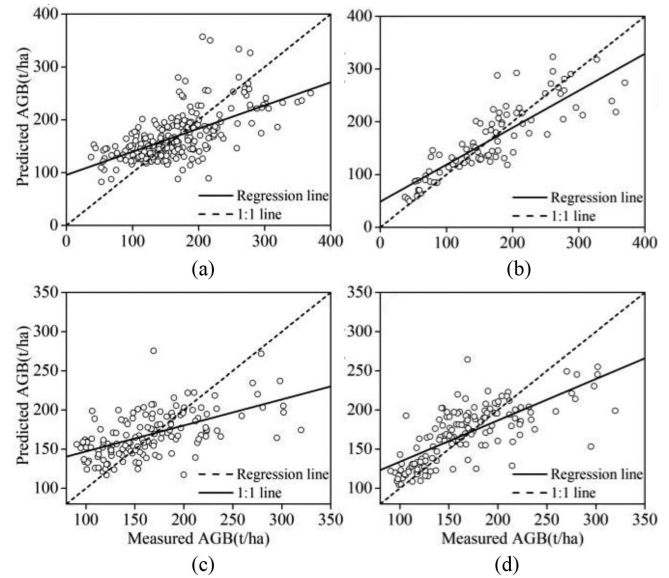

Fig. 6. Scatter diagram of RF regression models between field-measured AGB and predicted AGB. (a) From all samples combined by collection years without DSM. (b) From samples without DSM in 2010. (c) From samples in 2016 without DSM. (d) From samples in 2016 with DSM.

TABLE VI
RMSE OF BIOMASS ESTIMATION AMONG DIFFERENT EXPERIMENTS BY USING WORLDVIEW-2 IMAGES AND RANDOM FORESTS

Experiments	Samples	Input features	RMSE (t/ha)	RMSE$_r$ (%)
Combine all samples by collection years	Samples in 2010 and 2016	Bands, VIs, and species	50.99	30.48%
Separate samples by collection years	Samples in 2010	Bands, VIs, and species	41.03	24.31%
	Samples in 2016	Bands, VIs, and species	38.92	23.40%
	Samples in 2016	Bands, VIs, species, and DSM	34.16	20.54%

models. All constructed models had consistent results. The most important input variables were DSM and species-type variables, with the red-edge band (B6) and associated VIs (mRE-SRI$_{651}$) being the next most important variables. Other variables exhibited inconsistent performance.

D. Spatio-Temporal Distribution of Mangrove Biomass

Fig. 8 shows the spatial distribution of mangrove biomass for different samples and input features. *K. candel* had consistently larger biomass and smaller gradient changes than *S. apetala*, and *S. apetala* also exhibits a biomass gradient from inshore to sea for models with separate samples [see Fig. 8(a) and (d)] in both 2010 and 2016. However, it was not the case when the samples from different years were combined [see Fig. 8(b) and (e)]. There was a more significant biomass trend for those including DSM as input [see Fig. 8(c)] than for those without DSM (see Fig. 8(d).

Comparing biomass maps from the highest accuracy models for 2010 and 2016 [see Fig. 8(a) and (c), respectively], it can be observed that *K. candel* AGB distribution decreased over the
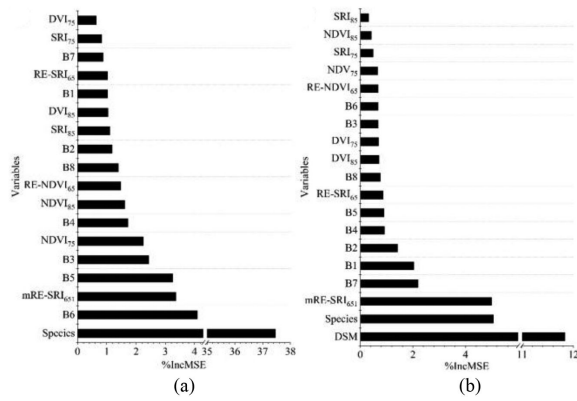
Fig. 7. Importance levels of the variables employed in the RF models for (a) 2010 and (b) 2016.
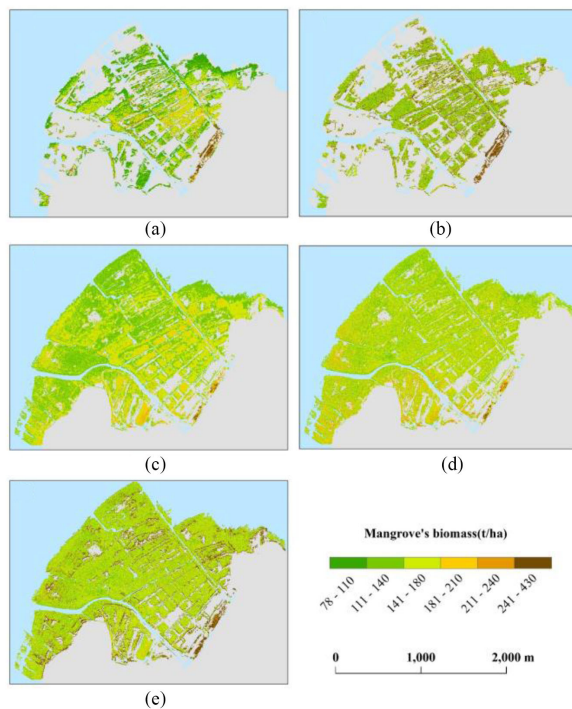

Fig. 8. Mangrove biomass maps for the study area generated by the biomass models. (a) 2010 map using 2010 samples only. (b) 2010 map using all samples. (c) 2016 map using DSM and 2016 samples. (d) 2016 map using only 2016 samples. (e) 2016 map using DSM and all samples.

period. Although previously planted *S. apetala* in 2010–2016 had higher AGB, newly planted vegetation during this period was the opposite. Models of combination samples from both years did not show this trend [see Fig. 8(b) and (e)].

V. DISCUSSION

A. Mangrove Biomass Distributions

Field investigation showed that *K. candel* AGB was significantly larger than *S. apetala*. This finding is consistent with Wang *et al.* [70], mainly because the native *K. candel* had higher growth density than *S. apetala*. However, the growth of *K. candel* was relatively slow between 2010 and 2016 due to their top communities and high density. *K. candel* was also caused to

blight, death, and photosynthesis inhibition from *D. trifoliata* cover; hence, AGB and density gradually reduced over the study period.

S. apetala had the largest growing area in the study area. This is a fast-growing species achieving a 1.5–3 m height increase in a year, which is related to AGB growth with age [15]. However, after approximately five years, the growth slowly stabilizes and plant density gradually decreases with age, mainly due to space and resource competition, causing some trees to stop growing and/or die [15], [71]. In this study, *S. apetala* mean AGB in 2016 was greater than in 2010, but restoration, i.e., planting, continued throughout the study period, and *S. apetala* exhibited a significant increase in area, although newly planted tree biomass was smaller than the older trees. Consequently, mean AGB in 2016 was slightly higher than in 2010. The artificially planted trees (*S. apetala*) occurred from the middle to low intertidal zones, and trees in medium tidal zones exhibited greater biomass compared to those in other locations.

B. Biomass Estimate Models

DSM was identified as the most important variable by the RF algorithm, and biomass models exhibited up to 3.14% (RMSEr) improved accuracy when including DSM compared to the equivalent model without DEM. The results were consistent with previous studies that remote sensing-based models of biomass including DSM or tree height variables are capable of improving estimate accuracies [24], [72]–[74]. Compared with the biomass maps in Fig. 8(c) and (d), the species of *K. candel* had similar biomass distribution in 2010 and 2016 [compare Fig. 8(c) and (d)], whereas *S. apetala* that was already present in 2010 showed higher biomass in 2016 and significantly more than new plantations. Models that included DSM input also produced better agreement with field investigation data. This was mainly because mangrove forests mainly occurred in intertidal zones without any undulating terrain conditions, i.e., relatively stable DEM, and hence, DSM derived from UAV images could effectively measure relative tree height.

This study found that the red edge band (B6) or the associated VIs (e.g., mRE-SRI$_{651}$) were the next-most important variables over other bands in estimating AGB. The results followed previous studies [51], [75]. That is mainly because the red edge band of WorldView-2 images was considered more sensitive to biomass than other traditional bands (e.g., the near-infrared band). A slight change of vegetation parameters will lead to a notable shift in the red edge band. However, optical images cannot provide tree height, which is one of the most important factors for estimating vegetation biomass [76]. Models using optical image spectral features [see Fig. 8(d)] mainly considered vegetation spectrum differences. However, optical images often incur saturation, causing underestimated high biomass due to multiple scattering in the canopy from dense vegetation [51]. Therefore, maps from models excluding DSM did not exhibit significant increases for existing vegetation between 2010 and 2016.

SfM photogrammetry was still considered an adequate low-cost technique for measuring forest stands. DSMs derived from
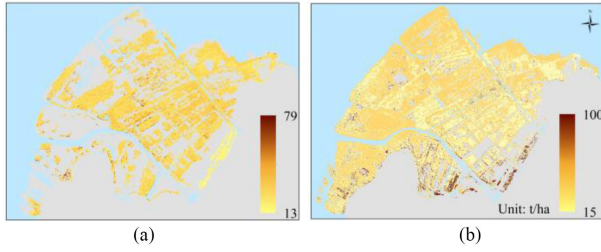
Fig. 9. Potential uncertainties of predicted AGB maps using the highest accuracy models in 2010 and 2016 by RMSE.

TABLE VII
BASIC STATISTICS OF MANGROVE BIOMASS OF THE MAPS GENERATED BY THE MODELS WITH THE HIGHEST ACCURACIES

K. candel					
Year	AGB average(t/ha)	Area(ha)	Total AGB(t)	AGB changes(t)	Change rates (%)
2010	263.21	2.92	768.57	-280.50	-36.50
2016	217.89	2.24	488.07		
S. apetala					
Year	AGB average(t/ha)	Area(ha)	Total ABG(t)	AGB change(t)	Change rates (%)
2010	128.15	175.59	22501.86	16829.10	74.79
2016	139.20	282.55	39330.96		

SFM and UAV photographs have high precision with less than 10 cm error [60]. Previous studies suggested that the uncertainties associated with the sensor calibration were less than the 2% of variable dynamic range and can be considered satisfactorily low [77]. However, point clouds from SfM and UAV photographs cannot penetrate dense forest canopies to get the actual tree height, which may cause the sources of uncertainties and error to propagate into the estimation of mangrove biomass. LiDAR with active remote sensing techniques can penetrate through the dense canopies and provide the accurate tree height datasets. Some studies have explored a comparison between LiDAR and SfM point clouds. The results suggested that both techniques can be used in relatively low canopy density, but the SfM photogrammetric technique underperformed LiDAR under increasingly denser canopy cover. Therefore, future studies should further consider using LiDAR techniques for biomass estimation [39], [78].

The most accurate AGB models [see Fig. 6(b) and (d)] show a higher AGB value and display higher RMSEs, indicating a statistical gradient of RMSE distribution. To get the reliability of the biomass per pixel, field plots were grouped into several AGB intervals at a 50 t/ha break using measured values [79]. RMSE was calculated for each interval in order to represent the uncertainties of the corresponding predicted AGB values (predicted maps). As shown in Fig. 9, the spatial distribution of potential AGB uncertainties was provided.

Since filed studies usually face physical obstacles in intertidal zones, we combined samples from different years to increase testing and training dataset sizes for developing biomass models. We compared AGB estimation based on different sample combinations using WorldView-2 images. The resulting models reach 30.48% of RMSEr within an acceptable range, but biomass maps were not consistent with field investigations and the mangrove plantation sequence [see Fig. 8(b) and (e)]. *K. candel* distribution was more reasonable since it remained relatively stable over the study period, but *S. apetala* distribution did not present the trends shown in more accurate models. This latter issue was due to seasonal differences between the images acquired in summer and autumn and *S. apetala* growth speed, causing large biomass and spectral feature differences between 2010 and 2016 images.

C. Mangrove Biomass Change Between 2010 and 2016

Table VII describes the mangrove biomass maps for the different species types from the most accurate models for 2010 and 2016 [see Fig. 8(a) and (c), respectively]. Total AGB in the study area increased from 23270.43 to 39819.03 tons by up to 71.11% between 2010 and 2016. The *K. candel* mean and total AGB decreased due to *D. trifoliata* incursion [70], and *S. apetala* increased 74.79% due to their faster growth rate and active forest plantation programs.

To further analyze the spatial and temporal changes of AGB of *S. apetala*, the species maps of two terms were performed intersection to extract unchangeable vegetation of *S. apetala* during 2010 and 2016. The results showed that the unchangeable area was 161.36 ha. Mean AGB increased from 121.15 to 146.41 t/ha between 2010 and 2016, i.e., 4.17 t/ha per year. Previous studies have shown annual AGB accumulation for *S. apetala* as high as 20.3 t/ha/y for 4–5-year-old stands, 5.60 t/ha/y for 5–8-year-old stands, and 2.85 t/ha/y for 8–10-year-old stands [14], [15]. *S. apetala* plantations have been artificially planted across the study area since 1999; hence, many stands have low AGB accumulation due to their higher tree age [14]. However, other stands were planted since 2008, because *Sonneratia caseolaris* plantations suffered from cold damage in 2008 and were gradually replaced by *S. apetala* plantings [52]. This study found mean AGB *S. apetala* accumulation for even-aged stands over the study period to be 4.17 t/ha, consistent with previous studies [14], [15].

VI. CONCLUSION

Estimating and mapping biomass dynamic change for mainly reforested areas at the species level is critical to accurately monitor the carbon stock dynamic of the coastal zone. Therefore, the goal of the study was to develop an effective and low-cost approach for applying remote sensing images to derive biomass change. In this study, we constructed AGB models with and without the consideration of DSM derived from the SfM algorithm applied to aerial photographs to evaluate effects on AGB estimation accuracy. We also evaluated the efficacy of including samples from different years to provide larger training and test datasets. Finally, spatio-temporal change of mangrove biomass was estimated and mapped based on built optimal models.

This study showed that models incorporating DSM information derived with the SfM algorithm exhibited up to 3.14% (RMSEr) improved accuracy for providing relative mangrove tree height from DSM data. The combined model from the entire

period from 2010 to 2016 increased relative error within an acceptable range, but enlarged training and test datasets. This method can be applied to estimate biomass changes, especially for limited samples. Total AGB in the study area increased by 71.11% between 2010 and 2016. Total AGB of native species decreased by 36.5% due to *D. trifoliata* coverage, whereas *S. apetala* total AGB increased by 74.79%, mostly due to the continuation of new plantations. AGB accumulation for unchanged *S. apetala* stands over the study period was 4.17 t/ha. These results provide valuable insights into biomass estimation models and vegetation recovery dynamics. Future studies should further consider using LiDAR techniques to obtain actual tree height applied for biomass estimation.

ACKNOWLEDGMENT

REFERENCES

[1] A. Ishtiaque, S. W. Myint, and C. Wang, "Examining the ecosystem health and sustainability of the world's largest mangrove forest using multi-temporal MODIS products," *Sci. Total Environ.*, vol. 569–570, pp. 1241–1254, 2016.

[2] X. Zhang *et al.*, "Mapping mangrove forests using multi-tidal remotely-sensed data and a decision-tree-based procedure," *Int. J. Appl. Earth Observ. Geoinf.*, vol. 62, pp. 201–214, 2017.

[3] D. C. Donato *et al.*, "Mangroves among the most carbon-rich forests in the tropics," *Nature Geosci.*, vol. 4, no. 5, pp. 293–297, 2011.

[4] V. Kankare *et al.*, "Retrieval of forest aboveground biomass and stem volume with airborne scanning LiDAR," *Remote Sens.*, vol. 5, no. 5, pp. 2257–2274, 2013.

[5] A. Abdul Aziz *et al.*, "Using REDD+ to balance timber production with conservation objectives in a mangrove forest in Malaysia," *Ecological Econ.*, vol. 120, pp. 108–116, 2015.

[6] N. Kosoy and E. Corbera, "Payments for ecosystem services as commodity fetishism," *Ecological Econ.*, vol. 69, pp. 1228–1236, 2010.

[7] J. A. A. Castillo *et al.*, "Estimation and mapping of above-ground biomass of mangrove forests and their replacement land uses in the Philippines using Sentinel imagery," *Int. Soc. Photogrammetry Remote Sens. J. Photogrammetry Remote Sens.*, vol. 134, pp. 70–85, 2017.

[8] C. Giri *et al.*, "Status and distribution of mangrove forests of the world using earth observation satellite data," *Global Ecol. Biogeography*, vol. 20, no. 1, pp. 154–159, 2011.

[9] Y. Zhu *et al.*, "Retrieval of mangrove aboveground biomass at the individual species level with worldview-2 images," *Remote Sens.*, vol. 7, no. 9, pp. 12192–12214, 2015.

[10] T. Jones *et al.*, "Madagascar's mangroves: Quantifying nation-wide and ecosystem specific dynamics, and detailed contemporary mapping of distinct ecosystems," *Remote Sens.*, vol. 8, no. 2, pp. 1–31, 2016.

[11] S. D. Sasmito *et al.*, "Remote sensing technique to assess aboveground biomass dynamics of mangrove ecosystems area in Segara Anakan, Central Java, Indonesia," in *Proc. 34th Asian Conf. Remote Sens.*, 2013, pp. 4560–4565.

[12] A. S. Ibrahim and T. G. Ngigi, "Assessment of mangrove spatial -temporal dynamics and biomass by remotely sensed data, case study Kilifi County: Kenya," *J. Geosci. Geomatics*, vol. 5, no. 1, pp. 24–36, 2017.

[13] L. T. H. Pham and L. Brabyn, "Monitoring mangrove biomass change in Vietnam using SPOT images and an object-based approach combined with machine learning algorithms," *Int. Soc. Photogrammetry Remote Sens. J. Photogrammetry Remote Sens.*, vol. 128, pp. 86–97, 2017.

[14] H. Ren *et al.*, "Biomass accumulation and carbon storage of four different aged Sonneratia apetala plantations in Southern China," *Plant Soil*, vol. 327, no. 1/2, pp. 279–291, 2010.

[15] H. Ren *et al.*, "Restoration of mangrove plantations and colonisation by native species in Leizhou bay, South China," *Ecological Res.*, vol. 23, no. 2, pp. 401–407, 2008.

[16] B. F. Clough and K. Scott, "Allometric relationships for estimating aboveground biomass in six mangrove species," *Forest Ecol. Manage.*, vol. 27, no. 2, pp. 117–127, 1989.

[17] A. Aslan *et al.*, "Mapping spatial distribution and biomass of coastal wetland vegetation in Indonesian Papua by combining active and passive remotely sensed data," *Remote Sens. Environ.*, vol. 183, pp. 65–81, 2016.

[18] C. Proisy, P. Couteron, and F. Fromard, "Predicting and mapping mangrove biomass from canopy grain analysis using Fourier-based textural ordination of IKONOS images," *Remote Sens. Environ.*, vol. 109, no. 3, pp. 379–392, 2007.

[19] N. R. Jachowski *et al.*, "Mangrove biomass estimation in Southwest Thailand using machine learning," *Appl. Geography*, vol. 45, pp. 311–321, 2013.

[20] H. Omar, M. Misman, and A. Kassim, "Synergetic of PALSAR-2 and Sentinel-1A SAR polarimetry for retrieving aboveground biomass in dipterocarp forest of Malaysia," *Appl. Sci.*, vol. 7, no. 7, pp. 1–20, 2017.

[21] T. R. Feldpausch *et al.*, "Tree height integrated into pan-tropical forest biomass estimates," *Biogeosci. Discuss.*, vol. 9, no. 3, pp. 2567–2622, 2012.

[22] L. Wang, J. L. Silván-Cárdenas, and W. P. Sousa, "Neural network classification of mangrove species from multiseasonal IKONOS imagery," *Photogrammetric Eng. Remote Sens.*, vol. 74, no. 7, pp. 921–927, 2008.

[23] M. K. Heenkenda *et al.*, "Mangrove species identification: Comparing worldview-2 with aerial photographs," *Remote Sens.*, vol. 6, no. 7, pp. 6064–6088, 2014.

[24] S. C. Popescu *et al.*, "Satellite LiDAR vs. small footprint airborne LiDAR: Comparing the accuracy of aboveground biomass estimates and forest structure metrics at footprint level," *Remote Sens. Environ.*, vol. 115, no. 11, pp. 2786–2797, 2011.

[25] A. Olagoke *et al.*, "Extended biomass allometric equations for large mangrove trees from terrestrial LiDAR data," *Trees*, vol. 30, no. 3, pp. 935–947, 2016.

[26] E. A. Feliciano *et al.*, "Estimating mangrove canopy height and aboveground biomass in the everglades national park with airborne LiDAR and TanDEM-X Data," *Remote Sens.*, vol. 9, no. 7, pp. 1–14, 2017.

[27] T. E. Fatoyinbo and M. Simard, "Height and biomass of mangroves in Africa from ICESat/GLAS and SRTM," *Int. J. Remote Sens.*, vol. 34, no. 2, pp. 668–681, 2013.

[28] T. E. Fatoyinbo *et al.*, "Landscape-scale extent, height, biomass, and carbon estimation of Mozambique's mangrove forests with Landsat ETM+ and shuttle radar topography mission elevation data," *J. Geophysical Res., Biogeosci.*, vol. 113, no. G2, pp. 1–13, 2008.

[29] M. Simard *et al.*, "Mapping height and biomass of mangrove forests in Everglades National Park with SRTM elevation data," *Photogrammetric Eng. Remote Sens.*, vol. 72, no. 3, pp. 299–311, 2006.

[30] J. P. Dandois and E. C. Ellis, "Remote sensing of vegetation structure using computer vision," *Remote Sens.*, vol. 2, no. 4, pp. 1157–1176, 2010.

[31] J. P. Dandois and E. C. Ellis, "High spatial resolution three-dimensional mapping of vegetation spectral dynamics using computer vision," *Remote Sens. Environ.*, vol. 136, pp. 259–276, 2013.

[32] J. Lisein *et al.*, "A photogrammetric workflow for the creation of a forest canopy height model from small unmanned aerial system imagery," *Forests*, vol. 4, no. 4, pp. 922–944, 2013.

[33] R. Jing *et al.*, "Above-bottom biomass retrieval of aquatic plants with regression models and SfM data acquired by a UAV platform—A case study in Wild Duck Lake Wetland, Beijing, China," *Int. Soc. Photogrammetry Remote Sens. J. Photogrammetry Remote Sens.*, vol. 134, pp. 122–134, 2017.

[34] M. A. Fonstad *et al.*, "Topographic structure from motion: A new development in photogrammetric measurement," *Earth Surface Processes Landforms*, vol. 38, no. 4, pp. 421–430, 2013.

[35] M. Maimaitijiang *et al.*, "Unmanned Aerial System (UAS)-based phenotyping of soybean using multi-sensor data fusion and extreme learning machine," *Int. Soc. Photogrammetry Remote Sens. J. Photogrammetry Remote Sens.*, vol. 134, pp. 43–58, 2017.

[36] M. J. Westoby *et al.*, "'Structure-from-Motion' photogrammetry: A low-cost, effective tool for geoscience applications," *Geomorphology*, vol. 179, pp. 300–314, 2012.

[37] I. Colomina and P. Molina, "Unmanned aerial systems for photogrammetry and remote sensing: A review," *Int. Soc. Photogrammetry Remote Sens. J. Photogrammetry Remote Sens.*, vol. 92, pp. 79–97, 2014.

[38] T. Ota *et al.*, "Aboveground biomass estimation using structure from motion approach with aerial photographs in a seasonal tropical forest," *Forests*, vol. 6, no. 12, pp. 3882–3898, 2015.

[39] L. Wallace *et al.*, "Assessment of forest structure using two UAV techniques: A comparison of airborne laser scanning and structure from motion (SfM) point clouds," *Forests*, vol. 7, no. 3, pp. 1–16, 2016.

[40] V. Otero *et al.*, "Managing mangrove forests from the sky: Forest inventory using field data and unmanned aerial vehicle (UAV) imagery in the Matang Mangrove Forest Reserve, peninsular Malaysia," *Forest Ecol. Manage.*, vol. 411, pp. 35–45, 2018.

[41] M. Jaud *et al.*, "Potential of UAVs for monitoring mudflat morphodynamics (Application to the Seine estuary, France)," *Int. Soc. Photogrammetry Remote Sens. Int. J. Geo-Inf.*, vol. 5, no. 4, pp. 1–20, 2016.

[42] J. Tian *et al.*, "Comparison of UAV and worldview-2 imagery for mapping leaf area index of mangrove forest," *Int. J. Appl. Earth Observ. Geoinf.*, vol. 61, pp. 22–31, 2017.

[43] X. Li *et al.*, "Regression and analytical models for estimating mangrove wetland biomass in South China using Radarsat images," *Int. J. Remote Sens.*, vol. 28, no. 24, pp. 5567–5582, 2007.

[44] J. Cao *et al.*, "Object-based mangrove species classification using unmanned aerial vehicle hyperspectral images and digital surface models," *Remote Sens.*, vol. 10, no. 1, pp. 1–20, 2018.

[45] D. Flanders, M. Hall-Beyer, and J. Pereverzoff, "Preliminary evaluation of eCognition object-based software for cut block delineation and feature extraction," *Can. J. Remote Sens.*, vol. 29, no. 4, pp. 441–452, 2003.

[46] V. Walter, "Object-based classification of remote sensing data for change detection," *Int. Soc. Photogrammetry Remote Sens. J. Photogrammetry Remote Sens.*, vol. 58, no. 3-4, pp. 225–238, 2004.

[47] W. R. Nascimento *et al.*, "Mapping changes in the largest continuous Amazonian mangrove belt using object-based classification of multisensor satellite imagery," *Estuarine, Coastal Shelf Sci.*, vol. 117, pp. 83–93, 2013.

[48] L. Wang, W. Sousa, and P. Gong, "Integration of object-based and pixel-based classification for mapping mangroves with IKONOS imagery," *Int. J. Remote Sens.*, vol. 25, no. 24, pp. 5655–5668, 2004.

[49] H. Zhang *et al.*, "Potential of combining optical and dual polarimetric sar data for improving mangrove species discrimination using rotation forest," *Remote Sens.*, vol. 10, no. 3, pp. 1–15, 2018.

[50] L. Breiman, "Random forests," *Mach. Learn.*, vol. 45, no. 1, pp. 5–32, 2001.

[51] O. Mutanga, E. Adam, and M. A. Cho, "High density biomass estimation for wetland vegetation using WorldView-2 imagery and random forest regression algorithm," *Int. J. Appl. Earth Observ. Geoinf.*, vol. 18, pp. 399–406, 2012.

[52] K. Liu *et al.*, "Exploring the effects of biophysical parameters on the spatial pattern of rare cold damage to mangrove forests," *Remote Sens. Environ.*, vol. 150, pp. 20–33, 2014.

[53] S. G. Wang *et al.*, "The change of mangrove wetland ecosystem and controlling countermeasures in the Qi'ao Island," *Wetland Sci.*, vol. 3, pp. 13–20, 2005.

[54] K. Liu *et al.*, "Monitoring mangrove forest changes using remote sensing and GIS data with decision-tree learning," *Wetlands*, vol. 28, no. 2, pp. 336–346, 2008.

[55] B. W. Liao *et al.*, "Studies on dynamic development of mangrove communities on Qi'ao Island, Zhuhai," *J. South China Agricultural University*, vol. 29, pp. 59–64, 2008.

[56] Q. J. Zan and Y. J. Wang, "Biomass and net productivity of sonneratia apetala, s.caseolaris mangrove man-made forest," *J. Wuhan Botanical Res.*, vol. 19, pp. 391–396, 2001.

[57] S. M. Seitz, B. Curless, J. Diebel, D. Scharstein, and R. Szeliski, "A comparison and evaluation of multi-view stereo reconstruction algorithms," in *Proc. IEEE Comput. Soc. Conf. Comput. Vis. Pattern Recognit.*, 2006, pp. 519–528.

[58] M. Kalacska *et al.*, "Structure from motion will revolutionize analyses of tidal wetland landscapes," *Remote Sens. Environ.*, vol. 199, pp. 14–24, 2017.

[59] T. Sankey *et al.*, "UAV LiDAR and hyperspectral fusion for forest monitoring in the southwestern USA," *Remote Sens. Environ.*, vol. 195, pp. 30–43, 2017.

[60] G. Forlani *et al.*, "Quality assessment of DSMs produced from UAV flights georeferenced with on-board RTK positioning," *Remote Sens.*, vol. 10, no. 2, pp. 1–22, 2018.

[61] F. Mancini *et al.*, "Using unmanned aerial vehicles (UAV) for high-resolution reconstruction of topography: The structure from motion approach on coastal environments," *Remote Sens.*, vol. 5, no. 12, pp. 6880–6898, 2013.

[62] G. L. David, "Distinctive image features from scale-invariant keypoints," *Int. J. Comput. Vis.*, vol. 60, no. 2, pp. 91–110, 2004.

[63] V. F. Rodriguez-Galiano *et al.*, "An assessment of the effectiveness of a random forest classifier for land-cover classification," *Int. Soc. Photogrammetry Remote Sens. J. Photogrammetry Remote Sens.*, vol. 67, no. 1, pp. 93–104, 2012.

[64] G. Ridgeway, "Generalized boosted models: A guide to the gbm package," *Update*, vol. 1, no. 1, pp. 1–15, 2007.

[65] A. Liaw and M. Wiener, "Classification and regression by randomForest," *R News*, vol. 2, no. 3, pp. 18–22, 2002.

[66] J. M. Peña-Barragán *et al.*, "Object-based crop identification using multiple vegetation indices, textural features and crop phenology," *Remote Sens. Environ.*, vol. 115, no. 6, pp. 1301–1316 2011.

[67] R. Pu and S. Landry, "A comparative analysis of high spatial resolution IKONOS and WorldView-2 imagery for mapping urban tree species," *Remote Sens. Environ.*, vol. 124, pp. 516–533, 2012.

[68] A. Abdul Aziz *et al.*, "Assessing the potential applications of Landsat image archive in the ecological monitoring and management of a production mangrove forest in Malaysia," *Wetlands Ecol. Manage.*, vol. 23, no. 6, pp. 1049–1066, 2015.

[69] Trimble. eCognition developer 9.0.1 reference book. 2014.

[70] Z. Wang *et al.*, "Study on Zhuhai Qi'ao Island main mangrove community characteristics," *J. Central South Univ. Forestry Technol.*, vol. 37, no. 4, pp. 86–91, 2017.

[71] A. Lunstrum and L. Chen, "Soil carbon stocks and accumulation in young mangrove forests," *Soil Biol. Biochem.*, vol. 75, no. 75, pp. 223–232, 2014.

[72] M. L. Clark *et al.*, "Estimation of tropical rain forest aboveground biomass with small-footprint LiDAR and hyperspectral sensors," *Remote Sens. Environ.*, vol. 115, no. 11, pp. 2931–2942, 2011.

[73] G. Vaglio Laurin *et al.*, "Above ground biomass estimation in an African tropical forest with LiDAR and hyperspectral data," *Int. Soc. Photogrammetry Remote Sens. J. Photogrammetry Remote Sens.*, vol. 89, pp. 49–58, 2014.

[74] S. Luo *et al.*, "Fusion of airborne LiDAR data and hyperspectral imagery for aboveground and belowground forest biomass estimation," *Ecological Indicators*, vol. 73, pp. 378–387, 2017.

[75] S. Adelabu *et al.*, "Spectral discrimination of insect defoliation levels in mopane woodland using hyperspectral data," *IEEE J. Sel. Topics Appl. Earth Observ. Remote Sens.*, vol. 7, no. 1, pp. 177–186, Jan. 2014.

[76] A. Komiyama, J. E. Ong, and S. Poungparn, "Allometry, biomass, and productivity of mangrove forests: A review," *Aquatic Botany*, vol. 89, no. 2, pp. 128–137, 2008.

[77] T. Miura, A. R. Huete, and H. Yoshioka, "Evaluation of sensor calibration uncertainties on vegetation indices for MODIS," *IEEE Trans. Geosci. Remote Sens.*, vol. 38, no. 3, pp. 1399–1409, May 2000.

[78] D. S. Cooper *et al.*, "Examination of the potential of terrestrial laser scanning and structure-from-motion photogrammetry for rapid nondestructive field measurement of grass biomass," *Remote Sens.*, vol. 9, no. 6, pp. 1–13, 2017.

[79] P. M. Montesano *et al.*, "The uncertainty of biomass estimates from LiDAR and SAR across a boreal forest structure gradient," *Remote Sens. Environ.*, vol. 154, pp. 398–407, 2014.
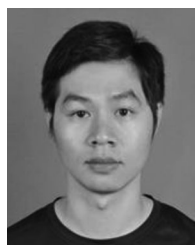
Yuanhui Zhu received the Ph.D. degree in cartography and geography information system from Sun Yat-sen University, Guangzhou, China, in 2017.

He is currently doing Postdoctoral research with the School of Geographical Sciences, Guangzhou University, Guangzhou, China. He is also with the Center of GeoInformatics for Public Security, Guangzhou, China. His research interests include vegetation remote sensing, concentrating on species classification, and estimation of biophysical parameters of mangrove wetlands using multispectral remote sensing images.

Kai Liu received the B.S. degree from the School of Geology Engineering and Geomatics from Chang'an University, Xi'an, China, in 2002, and the Ph.D. degree from the Guangzhou Institute of Geochemistry, Chinese Academy of Sciences, Guangzhou, China, in 2007.

He is currently an Associate Professor with the School of Geography and Planning, Sun Yat-sen University, Guangzhou, China. His research interests include wetlands, especially on mangrove and dyke pond system by using remote sensing and geographic information science technologies.

Lin Liu received the B.S. degree in geography and the M.S. degree in remote sensing and cartography from Peking University, Beijing, China, in 1984 and 1987, respectively, and the Ph.D. degree in geography with a specialization in geographic information science (GIS) from The Ohio State University, Columbus, OH, USA, in 1994.

He is currently a Professor of geography with the University of Cincinnati, Cincinnati, OH, USA, and Guangzhou University, Guangzhou, China. He has authored and co-authored more than 170 articles and led multiple national and international research projects. His research interests include GIS, remote sensing, and their applications.

Soe W. Myint received the Ph.D. degree in geography from Louisiana State University, Baton Rouge, LA, USA.

He is currently a Professor with the School of Geographical Sciences and Urban Planning, Arizona State University, Tempe, AZ, USA. He has more than 20 years of experience in remote sensing, GIS, geospatial statistics, spatial modeling, and geospatial classification algorithm development in an effort to inform our understanding of land cover land use (LCLU) change and simulation, drought, land degradation, desertification, agriculture water use, disaster management, assessment, and mitigation, land configuration, regional climate change, urban environmental modeling, assessment of deforestation and forest degradation, and coastal zone mapping.

Shugong Wang receive the Ph.D. degree in physical geography from Sun Yat-sen University, Guangzhou, China, in 2015.

He is currently with the School of Earth Sciences and Engineering, office of Scientific Research & Development, Sun Yat-sen University, Guangzhou, China. His research interests include the interdisciplinary geochemical research of the earth's surface, mainly focusing on the bio-geochemical cycling of coastal mangrove wetlands.

Jingjing Cao received the M.S. degree in cartography and geographic information system from Sun Yat-sen University, Guangzhou, China, in 2013. She is currently working toward the Ph.D. degree with the School of Geography and Planning, Sun Yat-sen University, Guangzhou, China.

Her current research interests include vegetation remote sensing, multisource remote sensing, and coastal environmental studies, concentrating on mangrove species classification, hyperspectral image analysis, unmanned aerial vehicle (UAV) remote sensing, and machine learning.

Zhifeng Wu received the Ph.D. degree in cartography and geography information system from the State Key Laboratory of Resource and Environmental Information System, Chinese Academy of Sciences, Beijing, China.

He is the Director of the School of Geographical Science, Guangzhou University, Guangzhou, China. He is also the Director of the Guangdong Provincial Engineering Technology Research Center for geographical conditions monitoring and comprehensive analysis. His research interests focus on urban remote sensing and human settlement environment.